Article

Timescale correlation of shallow trap states increases electrochemiluminescence efficiency in carbon nitrides

Yanfeng Fang[1,4], Hong Yang[1,4], Yuhua Hou[1], Wang Li[1], Yanfei Shen [2]✉, Songqin Liu[1] & Yuanjian Zhang [1,3] ✉

Highly efficient interconversion of different types of energy plays a crucial role in both science and technology. Among them, electrochemiluminescence, an emission of light excited by electrochemical reactions, has drawn attention as a powerful tool for bioassays. Nonetheless, the large differences in timescale among diverse charge-transfer pathways from picoseconds to seconds significantly limit the electrochemiluminescence efficiency and hamper their broad applications. Here, we report a timescale coordination strategy to improve the electrochemiluminescence efficiency of carbon nitrides by engineering shallow electron trap states via Au-N bond functionalization. Quantitative electrochemiluminescence kinetics measurements and theoretic calculations jointly disclose that Au-N bonds endow shallow electron trap states, which coordinate the timescale of the fast electron transfer in the bulk emitter and the slow redox reaction of co-reagent at diffusion layers. The shallow electron trap states ultimately accelerate the rate and kinetics of emissive electron-hole recombination, setting a new cathodic electrochemiluminescence efficiency record of carbon nitrides, and empowering a visual electrochemiluminescence sensor for nitrite ion, a typical environmental contaminant, with superior detection range and limit.

Over billions of years, organisms have evolved to become incredibly efficient in energy conversion. This efficiency is essential for life, as it allows organisms to grow, reproduce, and survive. For the same reason, highly efficient interconversion of different types of energy plays a crucial role in both science and technology. Among them, electrochemiluminescence (ECL), a type of light emission produced by electrochemical reactions in the vicinity of electrodes in solution[1–6], has been successfully commercialized in bioassays for more than 150 clinical biomarkers[7–15]. In general, ECL emitters of high efficiency (Φ_{ECL}) play a central role in developing biosensors with superior sensitivity. Nonetheless, due to the intricate kinetic limitations, Φ_{ECL} of most ECL emitters in aqueous solutions is essentially low.

To address this challenge, various innovative strategies have been proposed. For instance, accelerating electron transfer at interfaces among electrodes, emitters, and co-reactants via shortened distances[16,17], Schottky junctions[18], nanoconfinement effect[19], or catalytic effects[20] leads to a significantly improved Φ_{ECL} for a variety of emitters. Suppression of non-radiative relaxation[17,21–28] (e.g., by aggregation/crystallization, host-guest recognition, and ligand-induced assembly), and pre-oxidation/reduction of emitters[29,30] provide alternative routes to booster Φ_{ECL}. In principle, the physical and chemical properties of materials are intrinsically bestowed by interplays not only over different length scales but also at variable time scales. Typical ECL with co-reactants contains mixed multiple charge-transfer

[1]Jiangsu Engineering Research Center for Carbon-Rich Materials and Devices, Jiangsu Province Hi-Tech Key Laboratory for Bio-Medical Research, School of Chemistry and Chemical Engineering, Nanjing 211189, China. [2]Medical School, Southeast University, Nanjing 210009, China. [3]Department of Oncology, Zhongda Hospital, Southeast University, Nanjing 210009, China. [4]These authors contributed equally: Yanfeng Fang, Hong Yang.
✉e-mail: Yanfei.Shen@seu.edu.cn; Yuanjian.Zhang@seu.edu.cn

pathways, including electron transfer in bulk emitters, redox reactions at emitters/co-reactants interface, and electron transition between excited and ground states. Notably, however, there are huge timescale mismatches among them from picoseconds to seconds. From an overall perspective, although challenging, unambiguously revealing ECL kinetics of each process is decisive in extracting the rate-determining step and therefore making a timescale reconcilement of them would open a new methodology to further boost Φ_{ECL}. Nonetheless, to the best of our knowledge, a complete quantitative description and coordination of ECL kinetics for diverse charge transfer processes at different timescales have still been lacking.

Herein, we report a timescale coordination strategy to improve Φ_{ECL} of carbon nitrides (CN) by engineering shallow electron trap states via Au-N bond functionalization (Au$_x$-CN). For this purpose, a quantitative description of the complete charge transfer kinetics during the ECL of CN from the timescale of picosecond to second was developed, using operando electrochemical impedance spectroscopy (EIS), fs-transient absorption spectroscopy (TAS), transit open circuit photovoltage (OCP) and density functional theory (DFT) calculations. It was revealed the Au-N bonding activated new shallow electron trap states, which worked as

an electron sink in coordinating the timescale differences between the slow redox reaction at diffusion layers and fast electron transfer in bulk CN. Accordingly, more excited electrons and holes were produced, leading to a faster electron transition kinetics between excited and ground states. As a result, the timescale coordination strategy showed a four-fold enhancement of Φ_{ECL} for CN, setting a new cathodic Φ_{ECL} record in aqueous solution and co-reagent pathway.

Results

Synthesis and structural characterization of Au$_x$-CN photoelectrode

As a metal-free polymeric semiconductor, 2D carbon nitride (CN) has drawn increasing attention as a new generation of conjugated polymer-based ECL luminophore[18,31–33]. It demonstrates intriguing properties, such as abundant availability, high stability, excellent bio-compatibility, and record-level cathodic Φ_{ECL} among metal-free ECL emitters[34,35]. Herein we take the Au$_x$-CN as a model system to modulate the timescales of each ECL process of CN. The general procedures for CN and Au$_x$-CN photoelectrode preparation were shown in Fig. 1a. Briefly, a clean fluorine doped tin oxide (FTO) glass was immersed into

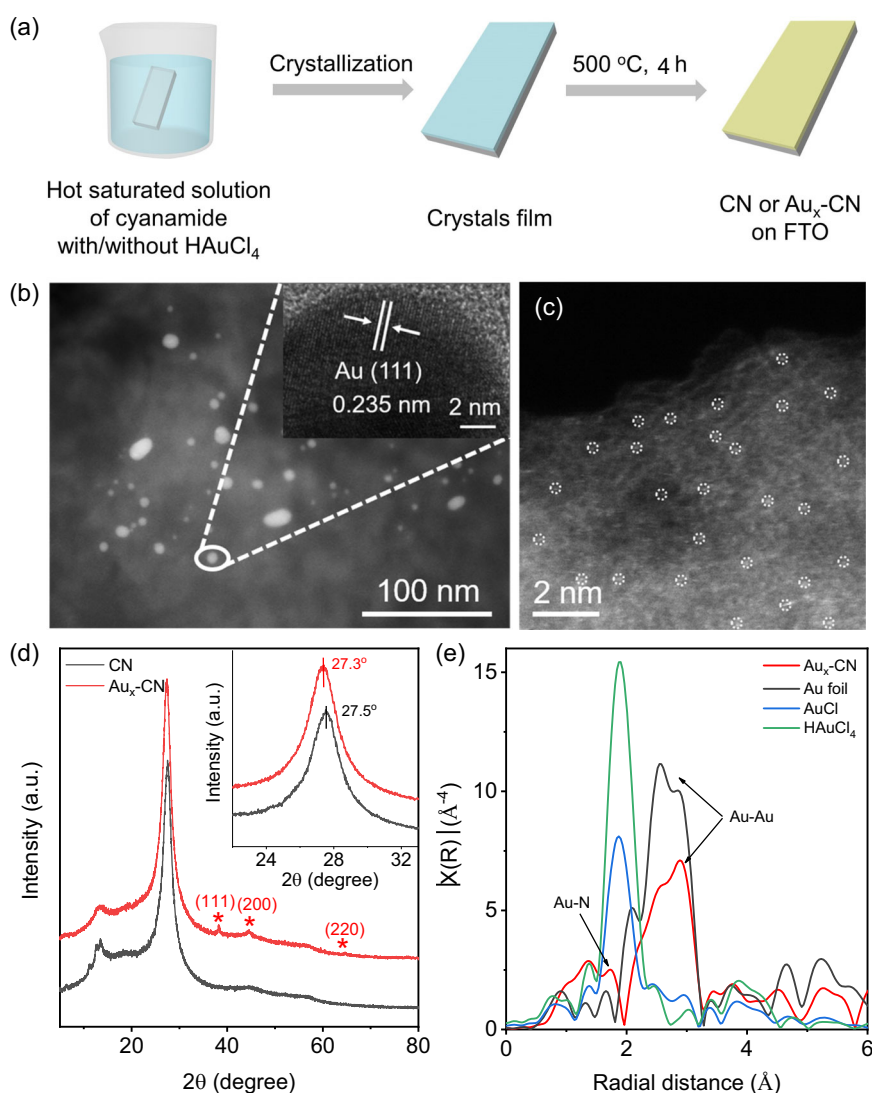**Fig. 1 | Synthesis and structural characterization of Au$_x$-CN photoelectrode.**
a Scheme of the general fabrication procedure for CN and Au$_x$-CN on the FTO.
b STEM and **c** HAADF-STEM images of Au$_x$-CN. Inset of **b**: HRTEM image of Au$_x$-CN. Isolated bright spots highlighted by a white circle: Au single atom. **d** XRD patterns of CN and Au$_x$-CN. The asterisk indicates the diffraction from Au nanoparticles. "a.u." refers to arbitrary units. **e** Fourier transforms of the EXAFS spectra of Au$_x$-CN and the reference samples.

a hot saturated cyanamide solution (80 °C) with or without $HAuCl_4$. A uniform crystal film was firmly coated on FTO after cooling. The final CN and Au_x-CN photoelectrodes were prepared by calcination of the crystal films at 500 °C for 4 h under N_2 atmosphere. The scanning electron microscopy (SEM) of CN and Au_x-CN photoelectrodes exhibited a continuous film on FTO with an intimate interface (Supplementary Fig. 1). Scratch-track morphologies showed no obvious cracks, indicating the good toughness of the CN and Au_x-CN photoelectrodes (Supplementary Fig. 2). To disclose the Au species in the interlayer of CN, the scanning transmission electron microscopy (STEM) images were measured. As shown in Figs. 1b and 1c, abundant bright spots were observed, corroborating the co-existence of uniformly dispersed Au nanoparticles (NPs) and single atoms in the adjacent layer of the CN matrix. High-resolution TEM (HRTEM) of Au_x-CN showed a typical Au (111) plane with a characteristic lattice spacing of 0.235 nm was observed (Fig. 1b inset)[18,36]. The corresponding high-resolution STEM-energy dispersive spectrometer (EDS) elemental mapping images showed that the C, N, and Au were homogeneously dispersed across the entire CN (Supplementary Fig. 3). The inductively coupled plasma-optical emission spectroscopy (ICP-OES) analysis showed that the Au loading in Au_x-CN was 0.06 wt %, indicating only a minor structural disorder was introduced into the pristine CN structure.

The layered crystal structures of Au_x-CN were investigated by X-ray diffraction (XRD, Fig. 1d). A series of characteristic diffraction peaks at $2\theta = 34.4°$, 44.7° and 64.8° belonging to (111), (200) and (220) crystal planes of Au NPs were slightly observed for Au_x-CN, further confirming the cubic crystal structure of the intercalated Au NPs[37]. Moreover, the XRD peak of Au_x-CN at 27.3° was observed, which could be assigned to interlayer stacking (002) of the conjugated aromatic systems[38]. Compared to that of CN (27.5°), it was shifted to a smaller angle, which was consistent with TEM analysis, indicative of a thicker interlayer distance due to intercalated Au species[39]. The Fourier transform infrared spectroscopy (FTIR, Supplementary Fig. 4), X-ray photoelectron spectroscopy (XPS, Supplementary Fig. 5) and matrix-free laser desorption/ionization time-of-flight mass (LDI-TOF-MS, Supplementary Fig. 6) spectra verified the intercalated Au rarely damaged the CN framework. The changes in the energy band structure were due to the incorporation of the Au species into CN (Supplementary Fig. 7).
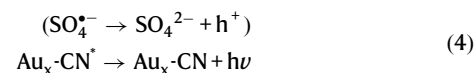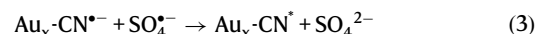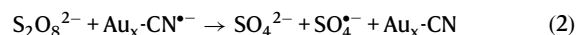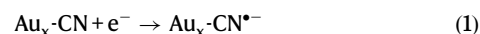
To explore the chemical state of Au in Au_x-CN, the X-ray absorption near-edge structure (XANES) spectroscopy was conducted at the Au L3-edge. As shown in Supplementary Fig. 8, the absorption edge for Au_x-CN was located between $HAuCl_4$ and Au foil references, and closer to that of AuCl, implying that the Au species carried slightly positive charges[40,41]. The valance state of Au_x-CN was further confirmed by the XPS spectra. Supplementary Fig. 9 showed the typical $4f^{5/2}$ and $4f^{7/2}$ signals at 89.7 and 83.4 eV, assigned to the oxidation state (Au^I) and metallic state (Au^0) in Au_x-CN[40], respectively. To disclose the coordination environment of Au species in Au_x-CN, the extended X-ray absorption fine structure (EXAFS) spectroscopy was investigated at the Au L3-edge. Figure 1e shows the Fourier transforms of the Au L3-edge EXAFS oscillations of the as-prepared Au_x-CN. It was obvious that the peaks at 2.0-3.3 Å were assigned to the Au-Au bond corresponding to Au NPs, while the peak located at approximately 1.7 Å could be ascribed to the scattering path of Au-N(C)[40,41]. According to this bond length, the density functional theory (DFT) calculation in the following discussion further verified that the Au-N bond was positioned between the interlayer of CN, rather than the cavity of the tri-s-triazine framework in the basal plane of CN. Therefore, by a simple co-polymerization method, Au-N bonding was introduced into the interlayer of CN.

ECL performance of Au_x-CN photoelectrode

As shown in Fig. 2a, a minor current in cyclic voltammogram (CV) curves were observed for both CN and Au_x-CN photoelectrode in the

solution without $K_2S_2O_8$, indicating negligible polarization of water during the reduction of $K_2S_2O_8$. Notably, the reduction peak of $K_2S_2O_8$ was out of the scope of the electrochemical window (Supplementary Fig. 10). It was attributed to the high iR drop of CN and Au_x-CN photoelectrode[42]. Figure 2b showed the ECL onset potential of Au_x-CN photoelectrode positively shifted by 200 mV compared to that of CN photoelectrode. As shown in Supplementary Fig. 11, different Au loadings were examined to assess the ECL intensity of the Au_x-CN photoelectrode, and the intensity reached almost 4 times that of the CN photoelectrode. The ECL of Au_x-CN photoelectrode was stable under continuous CV scans (Fig. 2c). The intense emission can be easily observed by the naked eyes and the uneven luminescence on the photoelectrodes may be attributed to differences in surface flatness after the thermal condensation (Fig. 2d). Figure 2e showed the ECL peak centered at ca. 455 nm, almost identical to the fluorescence (FL) spectrum, manifesting the CB-VB transition mechanism, different from many nanostructured ECL emitters with defective state emission[35,43]. An easily reproducible $Ru(bpy)_3^{2+}/K_2S_2O_8$ aqueous system was used as a reference to facilely compare Φ_{ECL} of different luminophores in this study (see the detailed discussion of the justification and calculation methods in the Experimental section of Supplementary Information and Supplementary Fig. 12 and 13). As shown in Fig. 2f, the Au_x-CN photoelectrode reached 3261 times the aqueous $Ru(bpy)_3^{2+}/K_2S_2O_8$ reference, which set a record of Φ_{ECL} for the CN family and was higher than those of most reported luminophores, to the best of our knowledge (Supplementary Table 1).

Electron transfer processes of ECL in Au_x-CN. The co-reactant typed ECL (e.g., $Ru(bpy)_3^{2+}$) has been elucidated in detail for four possible reaction routes (Supplementary Fig. 14)[44,45]. Three of them are involved in the direct oxidation of co-reactants on the electrode surface (Supplementary Fig. 14a-c). Especially, for the CN and Au_x-CN photoelectrode, the redox reaction was evidently inhibited by ca. 1000 times compared with bare FTO in regard to the interfacial charge transfer resistance across the electrode/electrolyte (R_{ct}, Supplementary Fig. 15 and Supplementary Table 2). It suggested that the co-reactants accepted electrons from CN or Au_x-CN, rather than the conventional substrate electrode. The general ECL mechanisms of Au_x-CN/$K_2S_2O_8$ system are shown in Eqs. (1)–(4)[35]. Briefly, electrons were injected from FTO substrate electrodes into the conduction band (CB) of CN to form Au_x-CN$^{•-}$ (Eq. (1)). Next, a few excited electrons obtained from Au_x-CN$^{•-}$ reduced co-reagents, producing strong oxidant $SO_4^{•-}$ (Eq. (2)), which subsequently generated holes in the valence band (VB, Eq. (3)) by an additional one-electron extraction. Lastly, the electrons in the CB and the holes in the VB recombined with the emission of light (Eq. (4)). The schematic illustration of charge transfer during ECL processes is shown in Fig. 3a.

$$Au_x\text{-}CN + e^- \rightarrow Au_x\text{-}CN^{•-} \tag{1}$$

$$S_2O_8^{2-} + Au_x\text{-}CN^{•-} \rightarrow SO_4^{2-} + SO_4^{•-} + Au_x\text{-}CN \tag{2}$$

$$Au_x\text{-}CN^{•-} + SO_4^{•-} \rightarrow Au_x\text{-}CN^* + SO_4^{2-} \tag{3}$$

$$(SO_4^{•-} \rightarrow SO_4^{2-} + h^+)$$
$$Au_x\text{-}CN^* \rightarrow Au_x\text{-}CN + h\nu \tag{4}$$

Electron transfer kinetics in bulk ECL emitters

To verify electron transfer in the bulk ECL emitter (Eq. 1), the EIS under different potentials, the fs-TAS, and the OCP were measured. Before that, the photothermal effect and the plasma resonance effect were excluded by control experiments, as negligible temperature variations
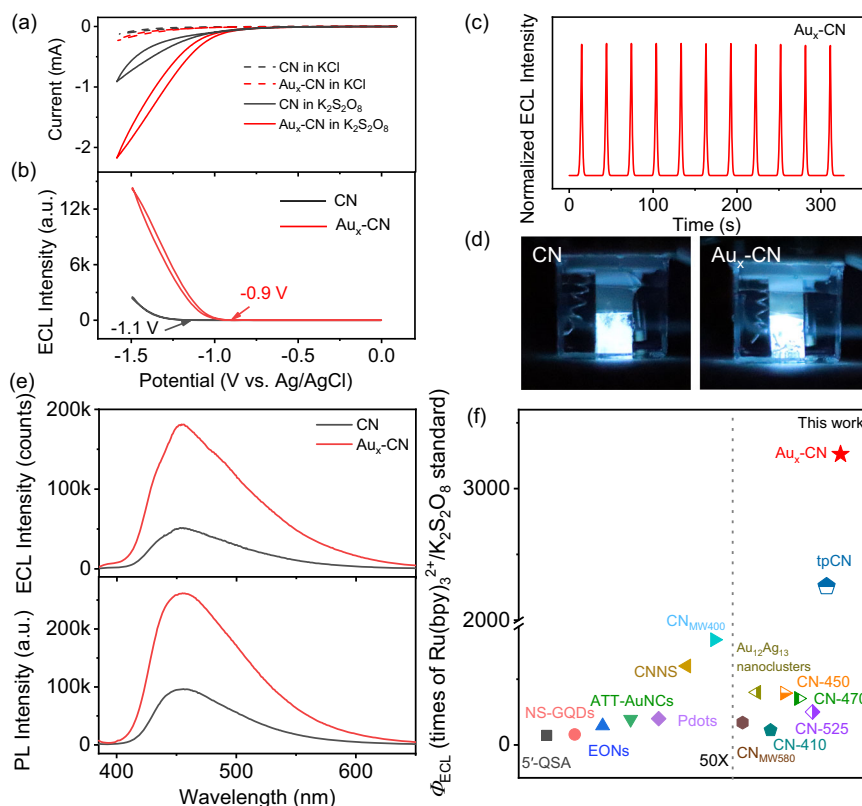
Fig. 2 | ECL performance of Au$_x$-CN photoelectrode. a CV and **b** ECL curves of CN and Au$_x$-CN photoelectrode. Electrolytes: 0.01 M phosphate buffer saline containing 0.1 M KCl with or without 25 mM K$_2$S$_2$O$_8$. "a.u." refers to arbitrary units. **c** ECL response of CN and Au$_x$-CN photoelectrode under continuous CV scans. **d** Photographs of CN and Au$_x$-CN photoelectrode under -1.5 V vs. Ag/AgCl. **e** ECL and fluorescence spectrum of CN and Au$_x$-CN photoelectrode. "a.u." refers to arbitrary units. **f** Relative ECL efficiency comparison of Au$_x$-CN photoelectrode and other counterparts in previous reports: 5'-QSA[78], NS-GQDs[65], EONs[79], ATT-AuNCs[21], CNNS[80], Pdots[16], CN$_{MW400}$[35], CN$_{MW580}$[42], Au$_{12}$Ag$_{13}$ nanocluster[81], CN-410[31], CN-450[31], CN-470[31], CN-525[31], tpCN[34]. The left panel divided by the dashed line shows magnified data (50x) and the data points to the left and right-hand side of the dashed line follow the same y scales.

(Supplementary Fig. 16) and plasma resonance effects of Au species (Supplementary Fig. 7b) were observed for the CN and Au$_x$-CN photoelectrodes. As shown in Fig. 3b, c, and Supplementary Fig. 17, at the low voltage, Nyquist plots revealed approximated straight lines, which indicated high charge reaction resistance. When the voltage increased, a more complete semicircle appeared in the Nyquist plots, suggesting the Faradaic reaction occurred[46,47]. Moreover, the CN and Au$_x$-CN photoelectrode started to exhibit Warburg impedance at −1.5 V and −1.0 V, respectively. The lower voltage value indicated that the CN photoelectrode had a limit in charge transfer resistance, presumably due to its poor electronic conductivity[46,47]. As shown in Fig. 3d, the Nyquist plots showed straight lines in the high-frequency part at −1.5 V. This type of EIS pattern belonged to the transmission line model (Supplementary Fig. 18)[48,49], and the simplified equivalent circuit models were shown in Fig. 3d inset (see the fit parameters in Supplementary Tables 3 and 4). As summarized in Supplementary Fig. 19, the values of electron transport resistance (R$_t$) remained almost constant under different applied voltages, indicating R$_t$ was an intrinsic property of emitters. The R$_t$ values for CN photoelectrode were approximately 5 times higher than that of Au$_x$-CN photoelectrode, suggesting the improved electron conductivity of Au$_x$-CN photoelectrode[47].

To confirm the carrier diffusion dynamics in bulk emitters, the carrier diffusion lifetime (τ$_d$) and electron mobility (μ) of CN and Au$_x$-CN photoelectrode at ECL work conditions were also analyzed from the EIS spectra. As shown in Fig. 3d, the inflection point between the straight line and arc in the high-frequency part was associated with τ$_d$, which was inversely correlated with the frequency[50,51]. The τ$_d$ of CN and Au$_x$-CN photoelectrode were calculated to be 99 and 39 μs, respectively. And the electron mobility was calculated using the Nernst-Einstein equation[51,52]:

$$\mu = \frac{eL^2}{k_B T \tau_d} \tag{5}$$

where e is the electronic charge, L is the effective travel distance of carriers through the active layer (3 μm in this work), k$_B$ is the Boltzmann constant, and T is the absolute temperature. The electron mobility of the Au$_x$-CN photoelectrode was calculated as 8.98 × 10^{-2} cm^2 V^{-1} s^{-1}, which was 3 times higher than that of the CN photoelectrode (3.54 × 10^{-2} cm^2 V^{-1} s^{-1}). The significantly reduced τ$_d$ and improved electron mobility of the Au$_x$-CN photoelectrode indicated the faster carrier diffusion kinetics in the bulk Au$_x$-CN photoelectrode. Therefore, in the bulk CN, electron diffusion kinetics was boosted after the introduction of the Au-N bond in the interlayer of CN.

To investigate the electron states in bulk emitters, the fs-TAS was conducted. Figure 3e exhibited a positive absorption from 500 to 780 nm and a negative absorption from 425 to 500 nm in the fs-TAS of CN and Au$_x$-CN photoelectrode at 5 fs delays under a 365 nm pump. The positive absorption features between 500 and 780 nm, which was highly related to photogenerated electrons in the CN[53,54]. The photo-induced absorption signal in the visible regions was partially quenched for Au$_x$-CN, indicative of an effective electron transfer between CN and Au species by Au-N bond[54]. To avoid the effects of excitation and emission, the kinetic courses of transient signals at 750 nm were used to study the electron transfer kinetics of CN and Au$_x$-CN photoelectrode[55]. The fitting results showed that the electron transfer lifetime (τ$_{ave-shallow}$) of CN and Au$_x$-CN photoelectrode were 185.48 and 348.99 ps, respectively (Fig. 3f). The quenched TAS intensity and
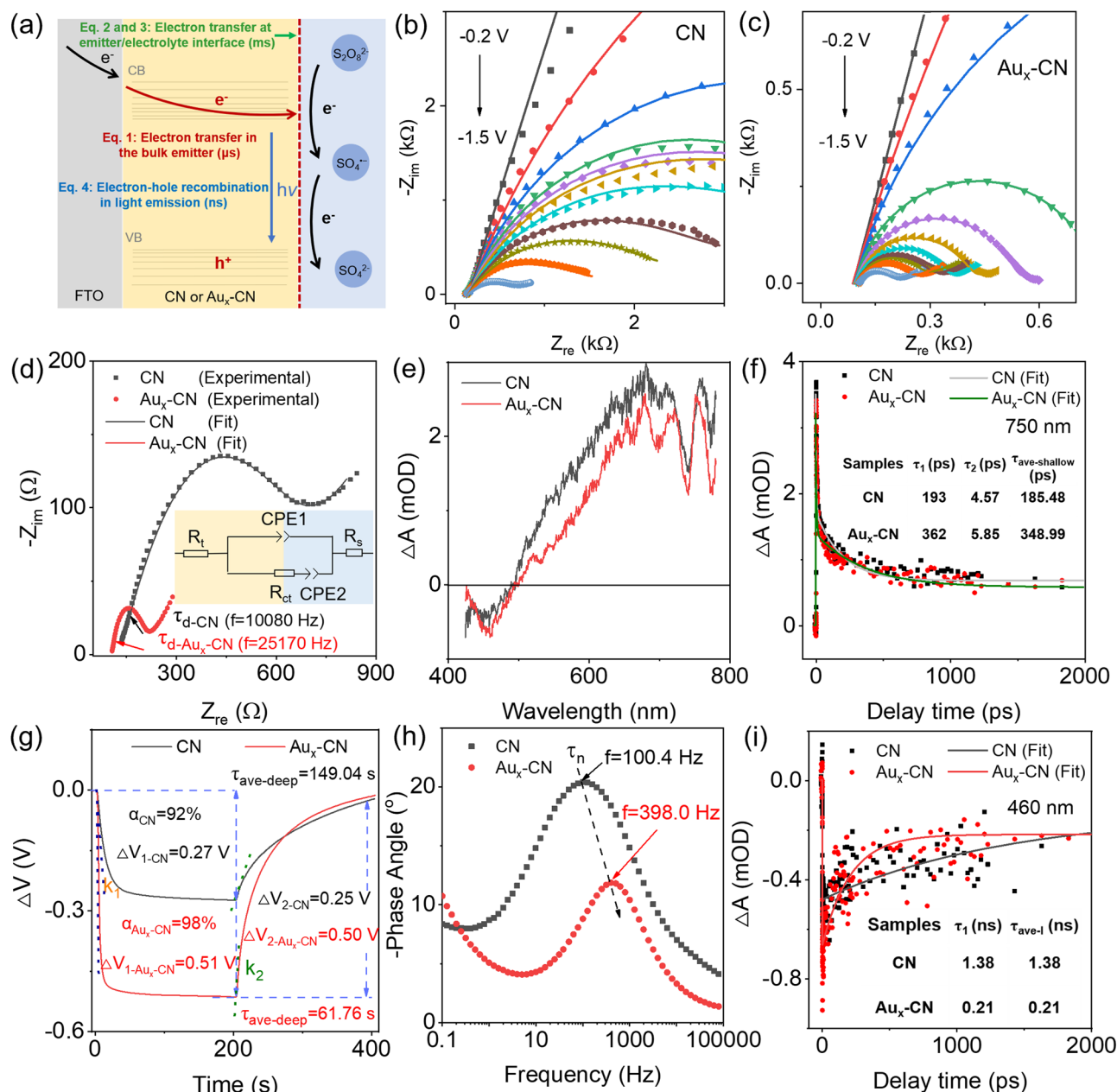
Fig. 3 | Electron transfer pathways and kinetics of Au$_x$-CN. a Possible charge transfer processes of ECL in Au$_x$-CN. Nyquist plots for **b** CN and **c** Au$_x$-CN photoelectrode at different applied potentials versus Ag/AgCl in 0.01 M phosphate buffer saline containing 0.1 M KCl and 25 mM K$_2$S$_2$O$_8$. Scatters and lines represent the experiment and fitted data, respectively. Black line: −0.2 V; Red line: -0.4 V; Blue line: −0.6 V; Green line: −0.8 V; Violet line: −0.9 V; Yellow line: −1.0 V; Cyan line: −1.1 V; Wine line: −1.2 V; Dark yellow line: −1.3 V; Orange line: −1.4 V; Light blue line: −1.5 V. **d** Nyquist plots for CN and Au$_x$-CN photoelectrode at −1.5 V vs. Ag/AgCl. Inset: Simplified equivalent circuit. R$_t$: electron transport resistance. R$_{ct}$: the charge reaction resistance. Constant phase element (CPE1): non-ideal capacitance. CPE2: non-ideal Warburg element. R$_s$: solution resistance. **e** Femtosecond transient absorption spectra of CN and Au$_x$-CN photoelectrode at 5 fs delays under a 365 nm pump. **f** Representative ultrafast transient absorption kinetics probed at 750 nm (pump at 365 nm) for CN and Au$_x$-CN photoelectrode. **g** Open circuit potential of CN and Au$_x$-CN photoelectrode under chopped visible light irradiation in 0.1 M KCl. ΔV$_1$ (arrow range): open circuit potential value after light on; ΔV$_2$ (arrow range): the recovery value of photovoltage after light off; k$_1$ (dashed line): the slopes of photovoltage drop after light on; k$_2$ (dashed line): the slopes of photovoltage drop after light off. **h** Bode plots for CN and Au$_x$-CN photoelectrode at −1.5 V vs. Ag/AgCl. **i** Representative ultrafast transient absorption kinetics probed at 460 nm (pump at 365 nm) for CN and Au$_x$-CN photoelectrode.

increased lifetime suggested that the near band-edge shallow electron trap states of CN, most presumably introduced/strengthened by Au-N bonding, offered more opportunities for excited electrons to participate ECL[55].

The OCP under chopped light was further measured to study the deep trapped long-lived electrons state (Fig. 3g). The surface deep electron trap state could be evaluated by the ratio of photovoltage value (α) after light on (ΔV$_1$) and off (ΔV$_2$). It is commonly believed that

low α is related to the electron deep trap state[42]. It was observed that the value of α was closer to 1 for Au$_x$-CN photoelectrode, suggesting a less surface-deep electron trap state. The average charge lifetime ($\tau_{ave-deep}$) was calculated by fitting the photovoltage decay curves[56,57]. As shown in Supplementary Fig. 20, the $\tau_{ave-deep}$ for CN photoelectrode was 149.04 s, which was 2 times of magnitude longer than Au$_x$-CN photoelectrode (61.76 s). In general, the long $\tau_{ave-deep}$ indicated severe electron trap effect[57]. Thus, the OCP measurement disclosed that

Au_x-CN photoelectrode had less surface deep trapping state of electrons, which would lead to a higher efficiency of electron utilization in ECL. Moreover, the OCP measurement disclosed that Au_x-CN photoelectrode had higher excited electron-storage capacity, which was favorable for excitation and faster electron-hole recombination kinetics (see more detailed discussion in Supplementary Fig. 21).

Electron transfer kinetics at emitter/co-reagent interface

The phase angle vs. frequency plots at different potentials (Supplementary Fig. 22) of CN and Au_x-CN photoelectrode were used to probe the co-reagent reduction kinetics at the emitter/$S_2O_8^{2-}$ interface during the ECL process (Eqs. (2) and (3)). The peak at the mediate frequency region is related to the effective lifetime[50,51] (τ_n, Fig. 3h). The τ_n of CN and Au_x-CN photoelectrode from EIS bode plots was approximately 4 times smaller than that of CN photoelectrode at different overpotentials (Supplementary Fig. 23) and the values of τ_n for CN and Au_x-CN photoelectrode was 9.9 ms and 2.5 ms at work conditions. In general, a shorter lifetime was associated with the faster electron transfer kinetic at the emitter/co-reagent interface. As shown in Supplementary Fig. 24, the R_{ct} for Au_x-CN photoelectrode obtained from EIS fitting was approximately 10 times smaller than that of CN photoelectrode at different overpotentials, indicating the reduction of $S_2O_8^{2-}$ was more ready to occur at the Au_x-CN/$S_2O_8^{2-}$ interface. Therefore, in the bulk CN, electron transfer kinetics at the emitter/co-reagent interface was boosted after the introduction of more efficient shallow electron trap states.

Electron-hole recombination kinetics in light emission. To understand the influencing factors for the emissive state in ECL (Eq. (4)), the fs-TAS, electron-hole recombination efficiency (η_{re}) and time-resolved FL spectra were measured. Figure 3e exhibited a negative absorption from 425 to 500 nm in the fs-TAS of CN and Au_x-CN photoelectrode, which was associated with the stimulated emission[54,56]. The lower TAS intensity indicated increased electron-hole recombination for Au_x-CN photoelectrode, which was consistent with the higher FL intensity in Fig. 2e. Accordingly, as shown in Supplementary Fig. 25, the calculated η_{re} (Eq. 6) of CN and Au_x-CN photoelectrode was calculated to be 47.0% and 65.6%. Moreover, the TA signal of Au_x-CN photoelectrode decreased to almost zero within 1 ns after photoexcitation, while that of CN did not, suggesting a fast electron-hole recombination (Supplementary Fig. 26)[56]. The fitting result of the negative signal was demonstrated in Fig. 3i. The electron-hole recombination lifetime (τ_l) of Au_x-CN photoelectrode fitted at 460 nm was 0.21 ns and this value was nearly 7 times shorter than that of CN photoelectrode (1.38 ns). Moreover, the FL decay lifetime for CN and Au_x-CN photoelectrode was also measured to be 3.46 ns and 1.69 ns, respectively (Supplementary Fig. 27). In general, a shorter TAS and FL decay lifetime of the radiative process often indicates a faster recombination rate for electron-hole pairs[42]. In this sense, the enhanced electron-hole recombination efficiency and decreased FL lifetime were observed, indicative of the critical role of the Au-N bond, most presumably via a more efficient shallow electron trap states.

$$\eta_{re}(\%) = \left(1 - \frac{J_{KCl}}{J_{TEOA}}\right) \times 100\% \qquad (6)$$

J_{KCl} is the photocurrent density obtained in 0.1 M KCl aqueous solution, while J_{TEOA} is the photocurrent density obtained in 0.1 M KCl containing 10% (v/v) triethanolamine (TEOA).

Given the above, the quantitative values of kinetic parameters for electron transfer in the ECL of CN and Au_x-CN are shown in Table 1. The roles of Au in the electron transfer in the ECL of Au_x-CN were summarized as follows. The formation of Au-N bonds accelerated the electron transfer in the bulk Au_x-CN photoelectrode. More importantly, it endowed new shallow electron trap states that had a longer lifetime, thus smoothing out the timescale inconsistencies of electron transfer at different stages. As shown in Table 1 and Supplementary

Fig. 28, the shallow-trapped electrons in the bulk emitter that existed at about the picosecond time scale ($\tau_{shallow}$) extended 2 times magnitude by the Au-N bond functionalization, which coordinated the slow charge transfer at the emitter/co-reactant interface in the millisecond time scale (τ_d) and fast electron transfer in bulk emitter in the microsecond time scale (τ_n). It would increase the reduction of co-reactants at the interface, and further improve the electron-hole recombination rate and efficiency for the ECL of Au_x-CN in the nanosecond time scale (τ_l). In contrast, the accumulation of long-lived, deeply trapped electrons in the second time scale (τ_{deep}), detrimental to efficient ECL, was effectively suppressed. It should be noted that while the intricate interplay of charge transfer kinetics in ECL has rarely been quantitatively dissected, the profound influence of charge carrier traps on ECL performance, despite their extensive exploration in organic semiconductors for diverse time scales, remains largely elusive. Harnessing quantitative kinetic study tools like operando EIS, transit OCP, and TAS, this study unveils how incorporating appropriate trap states can manipulate the timescales of substantial fluctuations in electron transfer within bulk ECL emitters, redox reactions at diffusion layers, and electron transitions between excited and ground states, thereby paving the way to enhance ECL efficiency.

Molecular insights of ECL enhancement by DFT calculations

The influence of Au-N bonds on accelerating the electron transfer and generating new shallow electron trap states in the Au_x-CN photoelectrode was explored by the DFT calculation. In a simplified Au_x-CN model (see Supplementary Fig. 29–34, see more discussion in Supplementary Information), the Au-N bonds, i.e., the distance between the Au atoms and the two adjacent CN layers, were 2.06 Å and 2.07 Å, respectively, matching well with the EXAFS results (Fig. 1e). The density of states (DOS) and the visible crystal orbitals of pristine CN and Au_x-CN were analyzed (Fig. 4). The valence band maximum (VBM) of pristine CN (Fig. 4a and c) mainly originated from the N 2p orbitals; whereas the conduction band minimum (CBM) was contributed both by the C and N 2p orbitals. A similar electronic structure of CBM was found in Au_x-CN (Fig. 4b and d), and the contribution from Au 5d and 6s orbitals was negligible; while the VBM was mostly formed by Au 5d and 6s orbitals and N 2p orbitals. As a result, the higher-energy Au 5d and 6s orbitals recombined with the pristine CN π bonding orbitals and π anti-bonding orbitals, which made the continuity of the energy band near the CBM and VBM in Au_x-CN be improved. Consequently, charge carriers could more readily transfer in the VBM and CBM, facilitating intralayer charge transfer.

In addition, inter-layer charge transfer was further analyzed by the Bader charge. The Bader charge difference between each adjacent layer of pristine CN was marginal (Supplementary Fig. 35b, $|\Delta q|$ roughly

Table 1 | Quantitative kinetic parameters of electron transfer in the ECL of CN and Au_x-CN

Electron transfer stage	Parameters	CN	Au_x-CN
In bulk ECL emitter	τ_d (μs)[a]	99	39
	μ (cm^2 V^{-1} s^{-1})[b]	3.54×10^{-2}	8.98×10^{-2}
	$\tau_{ave-shallow}$ (ps)[c]	185.48	348.99
	$\tau_{ave-deep}$ (s)[d]	149.04	61.76
At the emitter/co-reactant interface	τ_n (ms)[e]	9.9	2.5
During light emission	τ_l (ns)[f]	1.38	0.21
	η_{re} (%)[g]	47.0%	65.6%

[a]carrier diffusion lifetime; [b]electron mobility; [c]shallow electron trap state lifetime; [d]deep electron trap state lifetime; [e]effective lifetime; [f]electron-hole recombination lifetime; [g]electron-hole recombination efficiency.
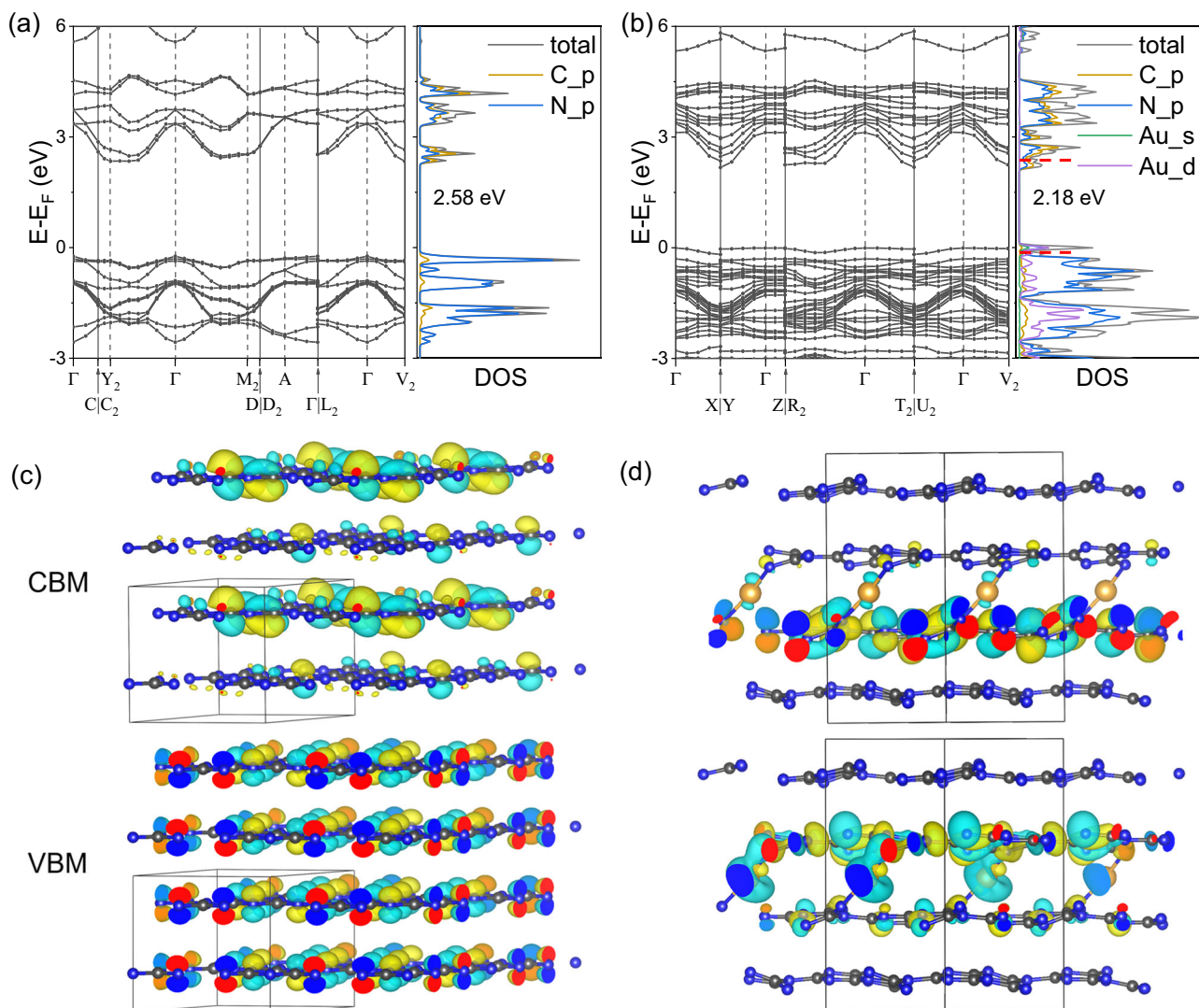
Fig. 4 | Band structure, DOS, and VBM/CBM crystal orbitals of CN and Au_x-CN. Band structure and DOS of **a** CN and **b** Au_x-CN. Red dash lines in Au_x-CN mark the positions of CMB and VBM for CN. VBM/CBM crystal orbitals of **c** CN and **d** Au_x-CN. Gray coloring indicates carbon atoms, blue indicates nitrogen, and orange indicates gold. Source data are provided as a Source Data file.

0.0009 e⁻), indicative of a very weak inter-layer charge transfer. In contrast, more electrons accumulated between each layer of Au_x-CN (Supplementary Fig. 35d, approximately 0.2 e⁻ of layer charge), and Au species lost 0.48 e⁻. As a result, Au_x-CN exhibited a much higher interlay charge difference (Supplementary Fig. 35d, $|\Delta q|$ roughly 0.142 e⁻ and 0.203 e⁻), indicating Au-N_x in the CN inter-layer served as a bridge, promoting the electron transfer between the adjacent layers. Thus, the Au-N bonding improved the overall electron transfer in Au_x-CN, compared to the pristine CN.

Considering that the Au content was only 0.06 wt% in the as-prepared Au_x-CN, the band structure in Au_x-CN should still be dominated by the pristine CN. Accordingly, the band gap of Au_x-CN was 2.79 eV, which was only 0.03 eV lower than the pristine CN (Supplementary Fig. 7). Nonetheless, the large-nuclear-charge Au species enhanced conjugation within the CN layer and made CBM shift down by 0.2 eV (red dash line in Fig. 4b). This new state close to the CBM energy level position of pristine CN, was usually considered to be shallow electron trap states, in which captured electrons could be released back to the band under external stimuli, such as an electric field, thereby reconciling the timescale difference of each step in ECL[58–60]. Therefore, the Au-N bonds not only accelerated the electron transfer in the bulk CN, but also created new shallow electron trap states near the CBM, two important factors in the improved ECL efficiency for CN.

Enhanced sensitivity in NO_2^- detection using Au_x-CN

The nitrite ion (NO_2^-), as a notorious pollutant, has gained significant interest due to its widespread presence in drinking water and various food products[61,62]. This prevalence has spurred intense research into the NO_2^- detecting. In general, NO_2^- could consume the $SO_4^{·-}$ around the electrode surface, resulting in a decrease of ECL intensity (Fig. 5a)[42]. Figure 5b and 5c showed that the cathodic ECL signal decreased gradually with the increase of NO_2^- concentration for both Au_x-CN and CN nanosheets photoelectrode. The logarithmic value of the ECL intensity at the Au_x-CN photoelectrode scaled linearly with the concentration of NO_2^- from 1×10^{-15} to 1×10^{-9} M, with a very low detection limit of 0.21 fM. The excellent performance of the NO_2^--based ECL biosensor has made it one of the most sensitive signal-amplification-free biosensors (Supplementary Table 5). As shown in Supplementary Fig. 36, the ECL intensity of the biosensor for detection of NO_2^- had little change under continuous potential scanning for more than 10 cycles, which indicated the good stability of the biosensor. And, the slope of the calibration curve and linear range of Au_x-CN photoelectrode exhibits more than
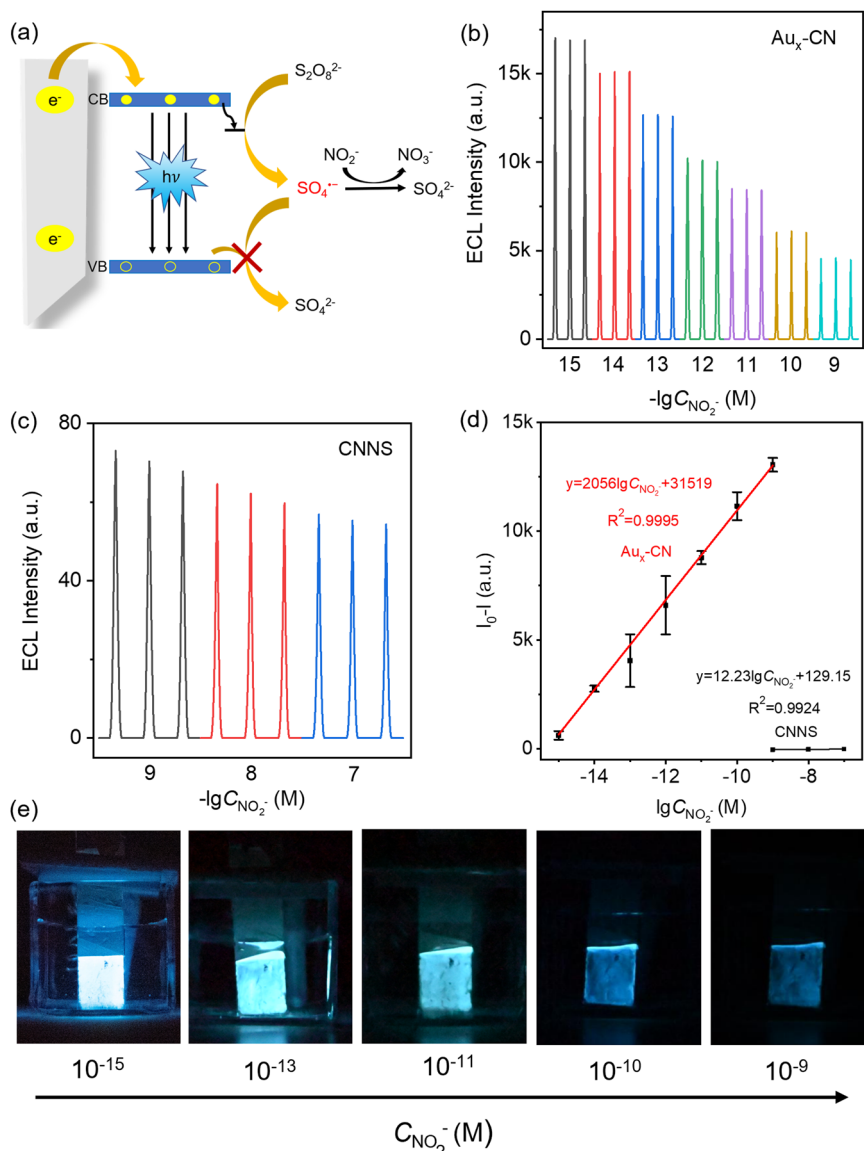
Fig. 5 | Nitrite sensor using CN and Au_x-CN. a ECL quenching mechanism upon NO_2^-. ECL curves in the presence of different concentrations of NO_2^- at **b** Au_x-CN and **c** CN nanosheets photoelectrode. Different colors indicate the concentrations indicated in the x-axis. "a.u." refers to arbitrary units. **d** Calibration curve of NO_2^- detection using Au_x-CN and CN nanosheets photoelectrode. I_0 and I are the ECL intensity before and after addition of NO_2^-, respectively. Error bars represent the standard error derived from three independent measurements. **e** Photographs of ECL at Au_x-CN photoelectrode in solution containing different concentrations of NO_2^-.

150-fold higher and 3 orders of magnitude than those of the control CN nanosheets (Fig. 5d). It suggested that the emitters with higher Φ_{ECL} held great potential in developing chemical sensors with superior sensitivity. Moreover, because of the exceptionally high cathodic ECL efficiency, it could be further developed into a visual cathodic ECL biosensor by naked eyes with uncompromising performance (Fig. 5e).

To explore the impact of doping other metals into CN on its ECL signal, the Ag_x-CN photoelectrode was synthesized by similar methods and conditions as that of Au_x-CN except that $HAuCl_4·4H_2O$ was replaced by $AgNO_3$. As shown in Supplementary Fig. 37, the ECL intensity of Ag_x-CN photoelectrode exhibits almost 5 times improvement compared to that of the undoped CN photoelectrode. This enhancement in ECL intensity may be attributed to the recombination of the d orbitals of the metals with the 2p orbitals of N atoms. The 5d orbitals of Au(I) were directly involved in the composition of the VBM (Fig. 4b), as another IB group metal Ag(I), the situation may be similar with Au(I).

Discussion

In summary, we report that the timescale coordination strategy remarkably improved the performance of ECL. The Au_x-CN photoelectrode demonstrated a four-fold enhancement of Φ_{ECL} for CN, setting a new cathodic Φ_{ECL} record of carbon nitrides in aqueous solution and co-reagent pathway (more than 3000 times that of the $Ru(bpy)_3Cl_2/K_2S_2O_8$ reference). Notably, this exceptionally high ECL performance ranks second only to core/shell II-VI quantum dots but the latter have critical biocompatibility and environmental concerns due to heavy metals. Operando EIS studies revealed that the Au_x-CN photoelectrode developed 2 times shorter carrier diffusion lifetime in microsecond timescale as compared to the CN photoelectrode. Furthermore, TAS revealed that, as compared to the CN photoelectrode, there was a large portion of electrons in shallow electron trap states in Au_x-CN and the lifetime of these electrons was extended by 2 times of magnitude into the picosecond timescale, which accelerated the slow $S_2O_8^{2-}$ reduction at the emitter/co-reactants interface with the timescale of millisecond by 4 times. Meanwhile, the average deep electron

lifetime observed for Au_x-CN photoelectrode was more than 2 times shorter than that of the CN photoelectrode in second timescale, which can be attributed to the faster electron transfer for Au_x-CN photoelectrode. Thus, the emissive electron-hole recombination rate and efficiency for Au_x-CN photoelectrode were promoted in nanosecond timescale.

As such, operando EIS, TAS, and transit OCP collectively provided evidence that the shallow electron trap states-induced timescale coordination associated with Au-N bonds were key to the ECL characterics of Au_x-CN photoelectrode. We ascribed the significant enhancement to a synergetic effect of the construction of Au-N bonds between CN layers, which provided the pathways for electron transfer to the photoelectrode/electrolyte interface. More importantly, the shallow trap state could act as an electron sink, which coordinated the timescale of the fast electron transfer in the bulk emitter and the slow redox reaction of co-reagent at diffusion layers, ultimately accelerating the recombination rate for electron-hole pairs and further promoting the ECL performance of Au_x-CN photoelectrode.

As a proof-of-concept application, Au_x-CN photoelectrode was successfully applied in a visual ECL sensor for a typical environmental contaminant, NO_2^-, with a wider detection range and lower detection limit, compared to the most previously studied CN nanosheets. Besides, except for the biosensing, carbon nitrides in bioimaging field could be envisaged. Due to its inherently high quantum yields, exceptional stability, excellent biocompatibility, and non-toxicity, the tunable ECL of carbon nitride holds potential for expanded applications in bioimaging[8,63,64]. The functionalization of carbon nitrides with diverse functional groups, which impart selective targeting capabilities, could facilitate the intracellular sensing of various analytes. The complete quantitative description of ECL kinetics and harnessing shallow electron trap states in timescale coordination of each step would expand the applicability of ECL emitters in various fields of optoelectronics devices, clinical diagnosis and bioimaging.

Methods

Reagents

Cyanamide (99%), and chloroauric acid ($HAuCl_4 \cdot 4H_2O$) were purchased from Energy Chemical, China. Potassium peroxodisulfate ($K_2S_2O_8$), potassium chloride (KCl), sodium dihydrogen phosphate dihydrate ($NaH_2PO_4 \cdot 2H_2O$), disodium hydrogen phosphate dodecahydrate ($Na_2HPO_4 \cdot 12H_2O$), sodium nitrite ($NaNO_2$), sodium borohydride ($NaBH_4$), methanol and triethanolamine (TEOA) were obtained from Shanghai Macklin Biochemical Co. Ltd., China. Gold nanoparticle (Au NPs, 10 nm) made by citric acid reduction method were purchased from Science Compass (China). Fluorine-doped tin oxide (FTO) glasses (12–14 Ω/sq, Zhuhai Kaivo Optoelectronic Technology Co., Ltd., China) were ultrasonically washed with acetone, ethanol, and ultrapure water for 15 min, respectively, and then dried with high purity nitrogen gas flow before use. Ultrapure water (18.2 MΩ·cm) was obtained from a Direct-Q 3 UV pure water purification system (Millipore, USA) throughout all experiments. Unless otherwise specified, all the other reagents were of analytical grade and used without further purification.

Characterization

Fourier-transformed infrared spectra (FTIR) were recorded using a Nicolet iS10 FT-IR spectrometer, equipped with an attenuated total reflection (ATR) setup (Thermo, USA). The structure of CN and Au_x-CN were characterized by matrix-free laser desorption/ionization time-of-flight mass (LDI-TOF-MS, AB Sciex 5800, USA). The morphology of CN, Au_x-CN, and the control Au/CN photoelectrode were investigated by FEI Inspect F50 scanning electron microscope (FEI, USA). The transmission electron microscopy (TEM) and energy dispersive spectrometer (EDS) of Au_x-CN were investigated by JEOL JEM-2100F and Oxford Instruments X-Max. The high-angle annular dark field scanning

transmission electron microscopy (HAADF-STEM) images were performed by JEM-ARM300F GRAND ARM. The mechanical properties of the CN and Au_x-CN films were tested using Bruker Hysitron TI98 (Bruker, USA). The XRD patterns were measured by using Ultima IV (Rigaku, Japan). The loadings of Au were measured on an inductively coupled plasma optical emission spectrometer (ICP-OES) on an Agilent 7800 (USA). X-ray photoelectron spectroscopy (XPS) was taken on a Scientific K-Alpha electron spectrometer (Thermo, USA) with monochromatic Al Kα X-rays (hv = 1486.6 eV) as the excitation source, and the binding energy was corrected by reference C 1s level to 284.6 eV to compensate for the specimen charging. The UV-vis absorption spectra were measured on a Cary 100 (Agilent, Singapore) with a diffuse-reflectance accessory, and $BaSO_4$ was used as a standard reference (100% reflectance). The fluorescence (FL) spectra and the time-resolved FL were performed on a Fluoromax-4 (Horiba Jobin Yvon, Japan). The fs-transient absorption spectra (fs-TAS) were carried out with a commercial transient absorption spectrometer (HELIOS, Ultrafast system) that includes a 1 kHz Solstice (New Corp.). A digital camera of Nikon Z5 (Nikon, Japan) equipped with the AstrHori 35 mm F/1.8 was used to take photographs of CN and Au_x-CN photoelectrodes under -1.5 V in Fig. 2d. The international standards organization (ISO), aperture size, and shutter speed were set at 51200, F1.8, and 1/60, respectively. Au L3-edge analysis was performed with Si (111) crystal monochromators at the BL11B beamlines at the Shanghai Synchrotron Radiation Facility (SSRF, Shanghai, China). Before the analysis at the beamline, samples were pressed into thin sheets with 1 cm in diameter and sealed using Kapton tape film. The XAFS spectra were recorded at room temperature using a 4-channel Silicon Drift Detector (SDD) Bruker 5040. Au L3-edge extended X-ray absorption fine structure (EXAFS) spectra were recorded in transmission mode. Negligible changes in the line shape and peak position of Au L3-edge XANES spectra were observed between two scans taken for a specific sample. The XAFS spectra of these standard samples (Au foil, AuCl, and $HAuCl_4$) were recorded in transmission mode. The spectra were processed and analyzed by the software codes Athena and Artemis.

Preparation of CN and Au_x-CN photoelectrode

The CN and Au_x-CN photoelectrode were obtained by the crystallization method. Briefly, 10 g cyanamide with or without $HAuCl_4 \cdot 4H_2O$ (10 μL, 500 mg/mL) was heated at 80 ℃ and melted. To deposit cyanamide crystal directly on the FTO glass, the clean FTO glass was immersed in a hot (80 °C) saturated cyanamide solution for 1 s and subsequently removed, yielding uniform crystal films on the FTO glass, which were then cooled naturally to room temperature. Finally, the crystal films were placed in a sealed glass tube and thermally condensed at 500 °C in a tube furnace (OTF-1200X-S, Hefei Kejing Materials Technology Co., Ltd, China) for 4 h in a N_2 atmosphere, and the as-obtained photoelectrodes were denoted as CN and Au_x-CN, respectively.

Preparation of Ag_x-CN photoelectrode

Ag_x-CN photoelectrode were synthesized by the similar methods and conditions as that of Au_x-CN except that $HAuCl_4 \cdot 4H_2O$ was replaced by $AgNO_3$.

Preparation of control Au/CN photoelectrodes

$NaBH_4$ reduction: Different concentrations of $HAuCl_4$ solution (1 nM-1 mM) was added to 8 mL of water containing the CN photoelectrode under stirring. Afterward, 48 μL of sodium citrate solution (0.01 M) was added dropwise into the suspension, followed by stirring for 30 min. Then, 120 μL of freshly prepared $NaBH_4$ solution (0.01 M) was added quickly to the above suspension and the stirring reaction was maintained for 20 min. Finally, the obtained Au_{NaBH4}/CN photoelectrode was immersed in ultrapure water to remove excess $NaBH_4$, sodium citrate, and unbound Au species.

Calcination: Different concentrations of $HAuCl_4$ solution (10 nM-1 mM) were dropwise to the above CN photoelectrode, then dried in a vacuum at 50 °C, followed by annealing at 300 °C in an N_2 atmosphere for 2 h. Finally, Au_{Cal}/CN was immersed in ultrapure water to remove excess unbound Au species.

Drop cast: A mixed solution of different volumes of Au NPs (2.5 μL-60 μL) and chitosan was dropwise to the CN photoelectrode, then dried in a vacuum at 50 °C. The Au_{NPs}/CN was immersed in ultrapure water to remove excess unbound Au NPs.

Photoreduction: A different concentration of $HAuCl_4$ solution (1 nM-1 mM) was added to 30 mL methanol containing the CN photoelectrode under stirring, followed by irradiating under a 150 W Xe light for 20 min. The Au_{photo}/CN was immersed in ultrapure water to remove excess unbound Au species.

Information of carbon nitride photoelectrodes

Thickness: ca. 300 nm; area: ca. 1 cm² and mass loading: 5 mg/cm².

ECL Measurements

The ECL intensity measurements were carried on an ECL analyzer system (MPI-E, Xi'an Ruimai Analytical Instruments Co. Ltd., China). The voltage of the photomultiplier tube (PMT) for collecting the ECL signal was biased at 100 V during detection.

Relative ECL efficiency determination: To compare ECL efficiency (Φ_{ECL}) with different luminophores, a facile $Ru(bpy)_3Cl_2/K_2S_2O_8$ aqueous system was used as a reference in this study. The ECL emission spectra were recorded by integrating CHI 400C with a Fluoromax-4 FL spectrophotometer, where the slit width was 3 nm. Φ_{ECL} was defined as the ratio of the number of photons produced per electron transferred between the oxidized and reduced analyte species relative to that of $Ru(bpy)_3Cl_2/K_2S_2O_8$, using Eq. (7)[65,66]:

$$\phi_{ECL} = \frac{\left(\frac{\int ECL\, dt}{\int Current\, dt}\right)_x}{\left(\frac{\int ECL\, dt}{\int Current\, dt}\right)_{st}} \times 100\% \qquad (7)$$

where "ECL" and "Current" represent integrated ECL photon numbers from the corrected ECL spectrum according to the count sensitivity of PMT at different light wavelengths and Faradaic electrochemical current values, respectively, "st" refers to the $Ru(bpy)_3Cl_2/K_2S_2O_8$ standard and "x" refers to the analyte. The potential was fixed at −1.5 V vs. Ag/AgCl by chronoamperometry in 0.01 M phosphate buffer saline (pH 7.4) containing 25 mM $K_2S_2O_8$ and 0.1 M KCl.

Calculation of photon counts: In this work, the spectrofluorometer coupled potentiostat was used as a high-resolution ECL spectrum acquisition system. As known, the recorded emission spectrum would be distorted by the response function of the PMT (sensitivity as a function of wavelength). In this sense, the variability in PMT's sensitivity to ECL emission at different wavelengths should be calibrated. In addition, the distance from the Au_x-CN photoelectrode or/ and GCE surface to the PMT surface and the Au_x-CN photoelectrode or/and GCE surface area were the same when collecting photons from the Au_x-CN photoelectrode and $Ru(bpy)_3{}^{2+}$.

Calculation of electrons: Unlike the Faradaic current, the non-Faradaic current during an electrochemistry process does not contribute to the ECL generation and should be subtracted when determining the intrinsic Φ_{ECL}. In this work, the potential was fixed at −1.5 V vs. Ag/AgCl by chronoamperometry instead of the CV curve when collecting the ECL emission spectrum. The charge consumed by Faraday processes, including $K_2S_2O_8$ and CN reduction in ECL, can be quantitatively evaluated by subtracting the charges consumed in electrolyte without $K_2S_2O_8$ from that with $K_2S_2O_8$. It was because the reduction of $K_2S_2O_8$ was performed on CN, which originally accepted electrons from the FTO substrate electrode. In the absence of $K_2S_2O_8$ in the electrolytes, only a

minor non-Faraday charging current of CN was observed (Fig. 2a). Such non-Faraday charging also exist during the reduction of $K_2S_2O_8$, and thus should be subtracted from the total consumed electrons. Lastly, at the beginning of the i-t curve for ECL reaction, the current drops rapidly within a few seconds, corresponding to the charging current. It does not contribute to the ECL generation. Therefore, the electron should be calculated after the i-t curve reaches a plateau.

As discussed in the reports by Ding and co-workers[66], the general utilization of 5% $Ru(bpy)_3{}^{2+}$ efficiencies that are not in acetonitrile, not with a rotating ring-disk electrode, not as the same concentration, or in co-reactant systems, has created poor comparisons to measured results for almost 4 decades. The measurement of absolute ECL efficiency (number of generated photons per occupied electrons) is the ultimate solution but requires sophisticated homemade instruments and future popularization.

In this sense, using a facile $Ru(bpy)_3Cl_2/K_2S_2O_8$ aqueous system under the same conditions as the reference would be a practical way to compare the relative ECL efficiency among different aqueous ECL systems. This method is also proposed by Ding and co-workers[65]. Nonetheless, it should be noted that the ECL intensity that is often measured by photomultiplier should be corrected when it is applied in Eq. (7), as the count sensitivity of photomultiplier varies significantly to lights at different wavelengths. Many previous reports ignored this key point. We adopted such a correction in this work, making the comparison of relative ECL efficiency for different carbon nitrides more reliable and reasonable[34,35,42].

In-situ electrochemical impedance spectroscopy (EIS) measurements

The in-situ electrochemical impedance spectroscopy (EIS) measurements were recorded in a Reference 600 potentiostat/galvanostat/ZRA (Gamry, USA). The potentials were measured against the Ag/AgCl (saturated KCl). EIS experiments were performed in a typical three-electrode system, consisting of CN or Au_x-CN photoelectrode, platinum wires, Ag/AgCl in saturated KCl as the working electrode, counter electrode, and reference electrode, respectively. EIS tests were performed using a 10 mV amplitude at different applied potentials versus Ag/AgCl in the frequency range of 0.1–100000 Hz. Electrolytes: 0.01 M phosphate buffer saline, 0.1 M KCl, and 25 mM $K_2S_2O_8$. In the simplified equivalent circuit model (Fig. 3d inset), R_t represented the resistivity of electron transport in the emitter film, which was the intrinsic resistance of the electrode materials. R_{ct} was the charge reaction resistance at the ECL emitter/$S_2O_8{}^{2-}$ interface, which was caused by the Faradaic reaction. The constant phase element (CPE) represented non-ideal capacitance, which was associated with the C_n. R_s was solution resistance. The suppressed semi-circle in high frequencies and straight line in low frequencies (<45°) implies that our system deviates from the most conventional model. The non-homogeneity and roughness structure of CN photoelectrode would influence the double-layer capacitance and semi-infinite diffusion of $S_2O_8{}^{2-}$ ions, respectively. To compensate for these non-ideal situations, the capacitor and Warburg element in the typical Randles circuit were replaced by two constant phase elements (CPE1 and CPE2)[67], as shown in Fig. 3d inset.

Photoelectrochemical measurements

All the electrochemical measurements were performed with a conventional three-electrode system, consisting of CN or Au_x-CN photoelectrode, platinum wires, Ag/AgCl in saturated KCl as the working electrode, counter electrode, and reference electrode, respectively. The photoelectrochemical (PEC) experiments were measured out in 0.1 M KCl at ambient conditions. The light source to simulate the sunlight was obtained from a 150 W Xe lamp and the average light intensity was 100 mW/cm². The open circus potential (OCP) was recorded in a Reference 600 potentiostat/galvanostat/ZRA (Gamry, USA). The potentials were measured against the Ag/AgCl (saturated KCl).

Computational methods

All theoretical calculations were performed based on DFT, implemented in the Vienna ab initio simulation package[68,69]. For the simulation of Au incorporated in the bulk phase of CN, a $1 \times 1 \times 2$ supercell of pristine bulk CN was adopted. And the k-points were sampled in a $3 \times 3 \times 2$ Monkhorst-Pack grid. The electron exchange and correlation energy were treated within the generalized gradient approximation in the Perdew-Burke-Ernzerh of functional[70,71]. The valence orbitals were described by plane-wave basis sets with cut-off energies of 500 eV. The atomic coordinates were fully relaxed using the conjugate gradient method[72]. The convergence criteria for the electronic self-consistent iteration was set to 10^{-5} eV. To quantitatively compare the degree of charge transfer, a Bader charge analysis has been carried out[73]. Electronic-structure calculations were performed using the hybrid functional HSE06 to avoid underestimating the band gap by the pure DFT method[74,75]. The electronic structures and density of states were generated using the VASPKIT script[76]. The crystal structures were visualized using VESTA software[77].

Finite element analysis

The simulations were performed using COMSOL Multiphysics (COMSOL Burlington, MA.). The transport of the diluted species (tds) module was used to simulate the electrochemical reaction that occurred on the electrodes is given by

$$S_2O_8^{2-} + 2e^- \rightleftharpoons 2SO_4^{2-} \tag{8}$$

Diffusion equations for $S_2O_8^{2-}$ and SO_4^{2-} are given by

$$\frac{\partial c_i}{\partial t} = D_i \left(\frac{\partial^2 c_i}{\partial x^2} \right) \tag{9}$$

where the diffusion coefficients of $S_2O_8^{2-}$ and SO_4^{2-}, D_i are taken as 1×10^{-5} cm²/s. The electron transfer rate of the reaction v_{et} is given by the Butler-Volmer model as

$$v_{et} = k_{red}c_{S_2O_8^{2-}} - k_{ox}c_{SO_4^-} \tag{10}$$

$$k_{red} = k_0 \exp\left[-\alpha F\left(E - E^{0'} \right)/RT \right] \tag{11}$$

$$k_{ox} = k_0 \exp\left[(1-\alpha)F\left(E - E^{0'} \right)/RT \right] \tag{12}$$

where k_{red} and k_{ox} are the reduction and oxidation rate constants, k_0 is the standard electron-transfer rate constant, α is the transfer coefficient, F is Faraday's constant, E is the electrode potential, $E^{0'}$ is the formal potential of the redox couple, R is the gas constant, and T is the temperature. For this reaction, α is taken as 0.5. For the simulation of the LSVs in this study, since the LSV occurs at negative potentials and the initial solution does not contain, Eq. 10 can be approximated as

$$k_{et} = k_0 \exp\left[-\frac{\alpha F\left(E - E^{0'} \right)}{RT} \right] c_{S_2O_8^{2-}} \tag{13}$$

which is further rearranged as

$$k_{et} = k_0 \exp\left[\frac{\alpha F E^{0'}}{RT} \right] \times \exp\left[-\frac{\alpha F E}{RT} \right] c_{S_2O_8^{2-}} = A \exp\left[-\frac{\alpha F E}{RT} \right] c_{S_2O_8^{2-}} \tag{14}$$

where $A = k_0 \exp\left[\frac{\alpha F E^{0'}}{RT} \right]$. Finally, a current response for LSV, i, is given by

$$i = nFSv_{et} \tag{15}$$

where n is the number of electrons transfer, and S is the surface area of electrodes.

Reporting summary

Further information on research design is available in the Nature Portfolio Reporting Summary linked to this article.

Data availability

The data supporting the conclusions of this study are present in the paper and the Supplementary Information. The raw data sets used for the presented analysis within the current study are available from the corresponding authors upon request. Source data are provided with this paper.

References

1. Ma, X. et al. Rational design of electrochemiluminescent devices. *Acc. Chem. Res.* **54**, 2936–2945 (2021).
2. Zanut, A. et al. Insights into the mechanism of coreactant electrochemiluminescence facilitating enhanced bioanalytical performance. *Nat. Commun.* **11**, 2668 (2020).
3. Cao, Z. et al. Unraveling mechanisms of highly efficient yet stable electrochemiluminescence from quantum dots. *J. Am. Chem. Soc.* **145**, 26425–26434 (2023).
4. Han, D. et al. Dynamic mapping of electrochemiluminescence reactivity in space: application to bead-based assays. *Anal. Chem.* **95**, 15700–15706 (2023).
5. Forster, R. J., Bertoncello, P., & Keyes, T. E. Electrogenerated chemiluminescence. *Annu. Rev. Anal. Chem.* **2**, 359–385 (2009).
6. Arcudi, F. et al. Lighting up the electrochemiluminescence of carbon dots through pre- and post-synthetic design. *Adv. Sci.* **8**, 2100125 (2021).
7. Dong, J. et al. Direct imaging of single-molecule electrochemical reactions in solution. *Nature* **596**, 244–249 (2021).
8. Liu, Y. et al. Single biomolecule imaging by electrochemiluminescence. *J. Am. Chem. Soc.* **143**, 17910–17914 (2021).
9. Lee, J. I. et al. Visco-poroelastic electrochemiluminescence skin with piezo-ionic effect. *Adv. Mater.* **33**, 2170222 (2021).
10. Sun, Q. et al. Ligand-induced assembly of copper nanoclusters with enhanced electrochemical excitation and radiative transition for electrochemiluminescence. *Angew. Chem. Int. Ed.* **62**, e202312053 (2023).
11. Yan, Y. et al. T cell antigen recognition and discrimination by electrochemiluminescence imaging. *Angew. Chem. Int. Ed.* **135**, e202314588 (2023).
12. Zhao, Y. et al. All-optical electrochemiluminescence. *J. Am. Chem. Soc.* **145**, 17420–17426 (2023).
13. Sun, R. et al. Highly electrochemiluminescent $Cs_4PbBr_6@CsPbBr_3$ perovskite nanoacanthospheres and their application for sensing Bisphenol A. *Anal. Chem.* **94**, 17142–17150 (2022).
14. Yang, X. et al. Gold microbeads enabled proximity electrochemiluminescence for highly sensitive and size-encoded multiplex immunoassays. *J. Am. Chem. Soc.* **145**, 16026–16036 (2023).
15. Sojic, N. *Analytical Electrogenerated Chemiluminescence: from Fundamentals to Bioassays*. Vol. 15 (Royal Society of Chemistry, 2019).
16. Wang, N. et al. Dual intramolecular electron transfer for in situ coreactant-embedded electrochemiluminescence microimaging of membrane protein. *Angew. Chem. Int. Ed.* **133**, 199–203 (2020).
17. Wang, T., Wang, D., Padelford, J. W., Jiang, J. & Wang, G. Near-infrared electrogenerated chemiluminescence from aqueous soluble Lipoic Acid Au nanoclusters. *J. Am. Chem. Soc.* **138**, 6380–6383 (2016).
18. Wu, Z. et al. Dual-site activation coupling with a Schottky junction boosts the electrochemiluminescence of carbon nitride. *Angew. Chem. Int. Ed.* **135**, e202308257 (2023).

19. Huang, X. et al. Direct visualization of nanoconfinement effect on nanoreactor via electrochemiluminescence microscopy. *Angew. Chem. Int. Ed.* **62**, e202215078 (2022).

20. Gu, W. et al. Single-atom iron boosts electrochemiluminescence. *Angew. Chem. Int. Ed.* **132**, 3562–3566 (2020).

21. Peng, H. et al. Dual enhancement of gold nanocluster electrochemiluminescence: electrocatalytic excitation and aggregation-induced emission. *Angew. Chem. Int. Ed.* **132**, 10068–10071 (2019).

22. Wong, J. M. et al. Revealing crystallization-induced blue-shift emission of a Di-Boron complex by enhanced photoluminescence and electrochemiluminescence. *Angew. Chem. Int. Ed.* **59**, 17461–17466 (2020).

23. Wei, X. et al. Aggregation-induced electrochemiluminescence of Carboranyl Carbazoles in aqueous media. *Angew. Chem. Int. Ed.* **58**, 3162–3166 (2019).

24. Guo, J. et al. Aggregation-induced electrochemiluminescence of Tetraphenylbenzosilole derivatives in an aqueous phase system for ultrasensitive detection of hexavalent Chromium. *Anal. Chem.* **92**, 14838–14845 (2020).

25. Ikeda, T. et al. Lewis-pairing-induced electrochemiluminescence enhancement from electron donor-acceptor diads decorated with Tris(pentafluorophenyl)borane as an electrochemical protector. *Angew. Chem. Int. Ed.* **62**, e202301109 (2023).

26. Zhu, Z. et al. Precise modulation of intramolecular aggregation-induced electrochemiluminescence by tetraphenylethylene-based supramolecular architectures. *Angew. Chem. Int. Ed.* **62**, e202312692 (2023).

27. Chu, K., Ding, Z. & Zysman-Colman, E. Materials for electrochemiluminescence: TADF, hydrogen-bonding, and aggregation- and crystallization-induced emission luminophores. *Chem. Eur. J.* **29**, e202301504 (2023).

28. Han, T. et al. Crystallization-induced enhanced electrochemiluminescence from a new Tris(bipyridine)ruthenium(II) derivative. *Adv. Funct. Mater.* **33**, 2212394 (2023).

29. Jin, Z. et al. Electroactive metal-organic frameworks as emitters for self-enhanced electrochemiluminescence in aqueous medium. *Angew. Chem. Int. Ed.* **132**, 10532–10536 (2020).

30. Peng, H. et al. Pre-oxidation of gold nanoclusters results in a 66% anodic electrochemiluminescence yield and drives mechanistic insights. *Angew. Chem. Int. Ed.* **131**, 11817–11820 (2019).

31. Fang, Y. et al. Highly efficient wavelength-resolved electrochemiluminescence of carbon nitride films for ultrasensitive multiplex MicroRNA detection. *Anal. Chem.* **95**, 6620–6628 (2023).

32. Chen, L. et al. Afterglow electrochemiluminescence from nitrogen-deficient graphitic carbon nitride. *Anal. Chem.* **95**, 2917–2924 (2023).

33. Zou, R., Lin, Y. & Lu, C. Nitrogen vacancy engineering in graphitic carbon nitride for strong, stable, and wavelength tunable electrochemiluminescence emissions. *Anal. Chem.* **93**, 2678–2686 (2021).

34. Hou, Y. et al. Growth of robust carbon nitride films by double crystallization with exceptionally boosted electrochemiluminescence for visual DNA detection. *Adv. Opt. Mater.* **11**, 2202737 (2023).

35. Zhao, T. et al. Ultrafast condensation of carbon nitride on electrodes with exceptional boosted photocurrent and electrochemiluminescence. *Angew. Chem. Int. Ed.* **59**, 1139–1143 (2019).

36. Wang, N. et al. Improving harsh environmental stability of few-layer black phosphorus by local charge transfer. *Adv. Funct. Mater.* **32**, 2203967 (2022).

37. Datta, K. K. R., Reddy, B. V. S., Ariga, K. & Vinu, A. Gold nanoparticles embedded in a mesoporous carbon nitride stabilizer for highly efficient three-component coupling reaction. *Angew. Chem. Int. Ed.* **49**, 5961–5965 (2010).

38. Zhou, Z. et al. Dissolution and liquid crystals phase of 2D polymeric carbon nitride. *J. Am. Chem. Soc.* **137**, 2179–2182 (2015).

39. Xiao, X. et al. A promoted charge separation/transfer system from Cu single atoms and C_3N_4 layers for efficient photocatalysis. *Adv. Mater.* **32**, 2003082 (2020).

40. Chen, Z. et al. Single-atom Au^I–N_3 site for acetylene hydrochlorination reaction. *ACS Catal.* **10**, 1865–1870 (2020).

41. Chen, Z. et al. Single-site Au^I catalyst for Silane oxidation with water. *Adv. Mater.* **30**, 1704720 (2017).

42. Fang, Y. et al. Elucidating orbital delocalization effects on boosting electrochemiluminescence efficiency of carbon nitrides. *Adv. Opt. Mater.* **10**, 2201017 (2022).

43. Wang, D., Gao, X., Jia, J., Zhang, B. & Zou, G. Valence-state-engineered electrochemiluminescence from Au nanoclusters. *ACS Nano* **17**, 355–362 (2022).

44. Miao, W., Choi, J.-P. & Bard, A. J. Electrogenerated Chemiluminescence 69: The Tris(2,2'-bipyridine)ruthenium(II), $(Ru(bpy)_3^{2+})$/Tri-n-propylamine (TPrA) system revisited a new route involving $TPrA^{·+}$ cation radicals. *J. Am. Chem. Soc.* **124**, 14478–14485 (2002).

45. Kerr, E., Doeven, E. H. & Francis, P. S. Recent advances in mechanistic understanding and analytical methodologies of the electrochemiluminescence of Tris(2,2'-bipyridine)ruthenium(II) and Tri-n-propylamine. *Curr. Opin. Electrochem.* **35**, 101034 (2022).

46. Zhang, N. et al. Electrochemical oxidation of 5-Hydroxymethylfurfural on Nickel Nitride/Carbon nanosheets: reaction pathway determined by in situ sum frequency generation vibrational Spectroscopy. *Angew. Chem. Int. Ed.* **58**, 15895–15903 (2019).

47. Xie, C. et al. In-situ phase transition of WO_3 boosting electron and hydrogen transfer for enhancing hydrogen evolution on Pt. *Nano Energy* **71**, 104653 (2020).

48. Bisquert, J. et al. Doubling exponent models for the analysis of porous film electrodes by impedance. relaxation of TiO_2 nanoporous in aqueous solution. *J. Phys. Chem. B* **104**, 2287–2298 (2000).

49. Mora-Sero, I., Garcia-Belmonte, G., Boix, P. P., Vázquez, M. A. & Bisquert, J. Impedance Spectroscopy characterisation of highly efficient silicon solar cells under different light illumination intensities. *Energy Environ. Sci.* **2**, 678–686 (2009).

50. Wang, Q., Moser, J.-E & Grätzel, M. Electrochemical impedance spectroscopic analysis of dye-sensitized solar cells. *J. Phys. Chem. B* **109**, 14945–14953 (2005).

51. Garcia-Belmonte, G. et al. Charge carrier mobility and lifetime of organic bulk heterojunctions analyzed by impedance Spectroscopy. *Org. Electron.* **9**, 847–851 (2008).

52. Jin, M.-J., Jo, J. & Yoo, J.-W. Impedance spectroscopy analysis on the effects of TiO_2 interfacial atomic layers in ZnO nanorod polymer solar cells: effects of interfacial charge extraction on diffusion and recombination. *Org. Electron.* **19**, 83–91 (2015).

53. Godin, R., Wang, Y., Zwijnenburg, M. A., Tang, J. & Durrant, J. R. Time-resolved spectroscopic investigation of charge trapping in carbon nitrides photocatalysts for hydrogen generation. *J. Am. Chem. Soc.* **139**, 5216–5224 (2017).

54. Corp, K. L. & Schlenker, C. W. Ultrafast spectroscopy reveals electron-transfer cascade that improves hydrogen evolution with carbon nitride photocatalysts. *J. Am. Chem. Soc.* **139**, 7904–7912 (2017).

55. Li, X. et al. Single-atom Pt as Co-catalyst for enhanced photocatalytic H_2 evolution. *Adv. Mater.* **28**, 2427–2431 (2016).

56. Ruan, Q., Miao, T., Wang, H. & Tang, J. Insight on shallow trap states-introduced photocathodic performance in n-type polymer photocatalysts. *J. Am. Chem. Soc.* **142**, 2795–2802 (2020).

57. Ruan, Q. et al. Key factors affecting photoelectrochemical performance of g-C_3N_4 polymer films. *Chem. Commun.* **55**, 7191–7194 (2019).

58. Mandal, S. et al. Extent of shallow/deep trap states beyond the conduction band minimum in defect-tolerant $CsPbBr_3$ Perovskite quantum dot: control over the degree of charge carrier recombination. *J. Phys. Chem. Lett.* **11**, 1702–1707 (2020).

59. Xue, J., Fujitsuka, M. & Majima, T. Shallow trap state-induced efficient electron transfer at the interface of heterojunction photocatalysts: the crucial role of vacancy defects. *ACS Appl. Mater. Interfaces* **11**, 40860–40867 (2019).

60. Haneef, H. F., Zeidell, A. M. & Jurchescu, O. D. Charge carrier traps in organic semiconductors: a review on the underlying physics and impact on electronic devices. *J. Mater. Chem. C.* **8**, 759–787 (2020).

61. Singh, L. & Ranjan, N. Highly selective and sensitive detection of nitrite ion by an unusual nitration of a fluorescent Benzimidazole. *J. Am. Chem. Soc.* **145**, 2745–2749 (2023).

62. Khachornsakkul, K., Del-Rio-Ruiz, R., Creasey, H., Widmer, G. & Sonkusale, S. R. Gold nanomaterial-based microfluidic paper analytical device for simultaneous quantification of gram-negative bacteria and nitrite ions in water samples. *ACS Sens* **8**, 4364–4373 (2023).

63. Zhang, J., Jin, R., Jiang, D. & Chen, H.-Y. Electrochemiluminescence-based capacitance microscopy for label-free imaging of antigens on the cellular plasma membrane. *J. Am. Chem. Soc.* **141**, 10294–10299 (2019).

64. Guo, W. et al. Potential-resolved multicolor electrochemiluminescence for multiplex immunoassay in a single sample. *J. Am. Chem. Soc.* **140**, 15904–15915 (2018).

65. Zhang, R., Adsetts, J. R., Nie, Y., Sun, X. & Ding, Z. Electrochemiluminescence of nitrogen- and sulfur-doped graphene quantum dots. *Carbon* **129**, 45–53 (2018).

66. Adsetts, J. R., Chu, K., Hesari, M., Ma, J. & Ding, Z. Absolute electrochemiluminescence efficiency quantification strategy exemplified with $Ru(bpy)_3^{2+}$ in the annihilation pathway. *Anal. Chem.* **93**, 11626–11633 (2021).

67. Lv, Y. et al. Competitive multiple-mechanism-driven electrochemiluminescent detection of 8-Hydroxy-2'-deoxyguanosine. *J. Am. Chem. Soc.* **140**, 2801–2804 (2018).

68. Kresse, G. & Furthmüller, J. Efficient iterative schemes forab initiototal-energy calculations using a plane-wave basis set. *Phys. Rev. B* **54**, 11169–11186 (1996).

69. Kresse, G. & Furthmüller, J. Efficiency of ab-initio total energy calculations for metals and semiconductors using a plane-wave basis set. *Comp. Mater. Sci.* **6**, 15–50 (1996).

70. Perdew, J. P., Burke, K. & Ernzerhof, M. Generalized gradient approximation made simple. *Phys. Rev. Lett.* **77**, 3865–3868 (1996).

71. Blöchl, P. E. Projector augmented-wave method. *Phys. Rev. B* **50**, 17953–17979 (1994).

72. Press, W. H., Teukolsky, S. A., Vetterling, W. T. & Flannery, B. P. *Numerical Recipes 3rd edition: The Art of Scientific Computing* (Cambridge University Press, 2007).

73. Yamakata, A., Ishibashi, T.-a & Onishi, H. Water- and oxygen-induced decay kinetics of photogenerated electrons in TiO_2 and Pt/TiO_2: A time-resolved infrared absorption study. *J. Phys. Chem. B* **105**, 7258–7262 (2001).

74. Heyd, J., Scuseria, G. E. & Ernzerhof, M. Hybrid functionals based on a screened coulomb potential. *J. Chem. Phys.* **118**, 8207–8215 (2003).

75. Paier, J. et al. Screened hybrid density functionals applied to solids. *J. Chem. Phys.* **124**, 154709 (2006).

76. Wang, V., Xu, N., Liu, J.-C., Tang, G. & Geng, W.-T. VASPKIT: A user-friendly interface facilitating high-throughput computing and analysis using VASP code. *Comput Phys. Commun.* **267**, 108033 (2021).

77. Momma, K. & Izumi, F. VESTA 3 for three-dimensional visualization of crystal, volumetric and morphology data. *J. Appl Crystallogr* **44**, 1272–1276 (2011).

78. Qin, X., Xu, X., Lu, J. & Zhu, Y. Highly efficient electrochemiluminescence of quinoline and isoquinoline in aqueous solution. *Electrochem Commun.* **101**, 19–22 (2019).

79. Li, S., Liu, Y. & Ma, Q. A novel polydopamine electrochemiluminescence organic nanoparticle-based biosensor for parathyroid hormone detection. *Talanta* **202**, 540–545 (2019).

80. Ji, J. et al. Simultaneous noncovalent modification and exfoliation of 2D carbon nitride for enhanced electrochemiluminescent biosensing. *J. Am. Chem. Soc.* **139**, 11698–11701 (2017).

81. Chen, S. et al. Near infrared electrochemiluminescence of rod-shape 25-Atom AuAg nanoclusters that is hundreds-fold stronger than that of $Ru(bpy)_3$ standard. *J. Am. Chem. Soc.* **141**, 9603–9609 (2019).

Acknowledgements

Author contributions

Y. Z. and Y. F. conceived and designed the experiments. Y. F. performed the synthesis, characterization, activity evaluation, mechanism studies, and sensor of CN and Au$_x$-CN photoelectrode. H. Y. performed the DFT calculation. Y. H. and W. L. assisted in the preparation of photoelectrodes. All authors contributed to the analysis and discussion of the results. Y. F., H. Y., and Y. Z. co-wrote the manuscript, and Y. Z., S. L., and Y. S. revised the manuscript. All authors reviewed the manuscript. Y. Z. supervised the project.

Competing interests

The authors declare no competing interests.

Additional information

Supplementary information The online version contains supplementary material available at https://doi.org/10.1038/s41467-024-48011-y.

Correspondence and requests for materials should be addressed to Yanfei Shen or Yuanjian Zhang.

Peer review information *Nature Communications* thanks Dechen Jiang, Jun-Jie Zhu and the other, anonymous, reviewer(s) for their contribution to the peer review of this work. A peer review file is available.

Reprints and permissions information is available at http://www.nature.com/reprints

Publisher's note Springer Nature remains neutral with regard to jurisdictional claims in published maps and institutional affiliations.